Intra-Network Synchronization and Retrodirective Distributed Transmit Beamforming with UAVs

Michael Wentz and Kaushik Roy Chowdhury, *Senior Member, IEEE*

***Abstract*—We propose and demonstrate a wireless communications system wherein multiple Unmanned Aerial Vehicles (UAVs) collaborate for Distributed Transmit Beamforming (DTBF) without feedback from the target receiver. This system can extend the collaborative downlink communications range without a single point of failure and allow the target to be agnostic to aspects of beamforming. However, it faces considerable challenges due to channel variations from the UAVs hovering and the need for timely and accurate synchronization. We devise an intra-network protocol using Gold codes for simultaneous channel sounding and fast frequency offset compensation among the UAVs. The received signal model is developed and compared to the case where receiver feedback is available. Statistical channel models for UAV hovering and oscillator stability are experimentally derived and used to evaluate the coherence time and beamforming performance at 915, 2550, and 5900 MHz. A prototype was implemented using software-defined radios and used to conduct the first demonstrations of DTBF without feedback in a mobile environment. Our experiments with two DJI M100 UAVs achieved convergence in 200 ms with beamforming gains over 90% of the theoretical maximum and within 10% of our modeling predictions, validating the proposed design.**

***Index Terms*—Distributed transmit beamforming, retrodirective beamforming, collaborative communications, UAVs.**

I. Introduction

ANTENNA arrays and beamforming have become key technologies for achieving higher data rates, reducing interference, and extending the range of wireless communications systems. There has been significant interest in forming arrays using distributed antenna elements [1]–[3], which offers advantages such as no single point of failure, the ability to scale and adapt on demand, and application to smaller platforms with payload constraints. These are desirable properties for Unmanned Aerial Vehicles (UAVs), since their downlink communications range R is limited by battery life [4] and typically requires a larger and more expensive UAV to increase. Alternatively, N smaller UAVs could use Distributed Transmit Beamforming (DTBF) to create a power gain of N^2 and extend the range to $N \times R$ for free-space channels [1]. This range extension is of particular interest for groups of UAVs used as aerial communications relays or base stations during emergency situations [5], for example as shown in Fig. 1. However, realizing these gains requires the UAVs to synchronize and coordinate at the radio frequency level, and ideally without additional hardware or modifications to existing target receivers.

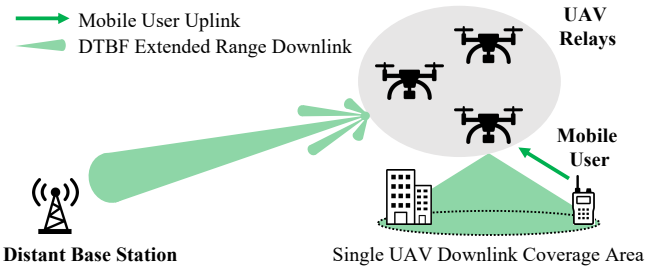

Fig. 1. UAVs deployed as part of an emergency network relay messages from a mobile user to a distant base station using DTBF for range extension.

• **Challenges in performing DBTF:** Synchronization of the UAVs is independent of the target and can be accomplished in-band [6] or with additional hardware [7]. However, coordination of their transmitter phases for DTBF depends on the positions of both the UAVs and the target. Movement of the UAVs changes the phases required for coherent combining at the target and necessitates periodic coordination to maintain the N^2 gain. For example, if one UAV in a 2.4 GHz DTBF system is displaced by 6.25 cm due to hovering, this induces a phase shift of 180° and leads to destructive interference. UAV movement also changes the beamwidth of the array, as it scales inversely with the distance between elements [1], and leads to narrower beams with greater sensitivity to phase errors when the UAVs are spaced further apart.

• **Motivation of proposed approach:** There are two architectures for coordinating the transmitter phases for DTBF: those that rely on a signal from the target and those that do not. Within the target informed architectures, the target may offer explicit feedback [8], [9] or broadcast a reference signal [6], [10]–[12]. Feedback requires the target be cognizant of beamforming and allocate both computational and protocol overhead. On the contrary, most wireless standards already

Manuscript received October 21, 2022; revised April 16, 2023; accepted August 16, 2023. Date of publication TBD; date of current version August 31, 2023.

DISTRIBUTION STATEMENT A. Approved for public release. Distribution is unlimited. This material is based on work supported by the Office of Naval Research under contract N00014-21-C-1111, NSF CNS 2229444, and the United States Air Force under contract FA8702-15-D-0001. Any opinions, findings, conclusions or recommendations expressed in this material are those of the authors and do not necessarily reflect the views of the United States Government.

The authors are with the Department of Electrical and Computer Engineering, Northeastern University, Boston, MA 02115 USA (e-mail: wentz.m@northeastern.edu, krc@ece.neu.edu). Michael Wentz is also with MIT Lincoln Laboratory, Lexington, MA 02421.

broadcast reference signals for synchronization and channel estimation. Re-using this signaling for DTBF with UAVs enables existing targets to be agnostic to beamforming but requires them to transmit. The second type of architecture has no dependence on the target transmitting and utilizes knowledge of relative positions [13], movement of an element [14], [15], or random alignment of unsynchronized transmitters [16]. The first of these requires a positioning system accurate to a fraction of the radio wavelength and would place additional burden on UAVs where typically only coarse positions are available. The second and third require either relatively slow movement of a UAV or repetition coding, both of which reduce the achievable data transfer for a given amount of time.

• **Overview of proposed approach:** In this paper, we propose Retrodirective DTBF (R-DTBF) using N UAVs for downlink range extension. The retrodirective technique exploits channel reciprocity by using the conjugate phases of the uplink channels for downlink beamforming on the same frequency [6], [17], [18], [20]. It requires no feedback from the target or position information, making it advantageous for emergency situations where the UAVs must be rapidly deployed and no assumptions can be made about the target supporting feedback for DTBF. However, it requires the target to transmit and be received by the UAVs, making the system most applicable to targets without stringent power constraints. Further, although channel reciprocity holds at the antennas, transmitter and receiver paths are generally non-reciprocal due to different components [21]. This can be compensated for by using indirect relative calibration and synchronization among the UAVs [12]. R-DTBF therefore requires the UAVs perform the following steps within the channel coherence time: (i) exchange messages for synchronization and calibration, (ii) receive a message from the target for channel estimation, and (iii) transmit with the coordinated phases for beamforming back to the target.

• **Paper contributions:** To design the system, we first developed a new R-DTBF protocol to minimize the time required for step (i), then analyzed the tolerable phase and frequency errors for the signal received during step (iii). Next, we conducted a series of experiments to derive statistical models for the channel phase variations due to UAV hovering and short-term oscillator stability, then applied the models to evaluate the performance of R-DTBF at 915, 2550, and 5900 MHz. Finally, we implemented a prototype using Software-Defined Radios (SDRs) and demonstrated the system with handheld antennas and on two DJI M100 UAVs. To the best of our knowledge, these were the first demonstrations of DTBF in a mobile environment without feedback from the target receiver. We achieved convergence in 200 ms with beamforming gains over 90% of the theoretical maximum and within 10% of our modeling predictions. In summary, our main contributions are:

- An R-DTBF protocol using Gold codes for simultaneous synchronization and calibration among distributed mobile platforms with short channel coherence times.
- A received signal model for the proposed protocol and comparison to DTBF with receiver feedback regarding the tolerance to phase errors.
- Experimentally derived models of the channel phase variations due to a UAV hovering while transmitting at 915, 2550, and 5900 MHz while using oscillators with varying degrees of stability. The performance of R-DTBF is evaluated under these models.
- Experimental validation of the proposed design in a mobile environment and with two UAVs. We achieved convergence in 200 ms, beamforming gains over 90% of the theoretical maximum, and results within 10% of our modeling predictions. Further, these results are from the first demonstrations of DTBF in a mobile environment without feedback from the target.

• **Outline:** The paper is organized as follows. Sec. II reviews current state-of-the-art and the shortcomings that we address. Sec. III defines the R-DTBF protocol and received signal model. System errors are analyzed in Sec. IV. Experimentally derived channel models for a hovering UAV are developed in Sec. V and used to evaluate the performance of R-DTBF in Sec. VI. Sec. VII describes our experimental validation using SDRs and UAVs. Sec. VIII discusses the results and practical considerations. We conclude in Sec. IX.

II. Related Work

As previously discussed, there are two architectures for DTBF: those that rely on a signal from the target receiver and those that do not. Depending on feedback from the target is a common approach [1]–[3], and examples include channel state feedback [8], [22]–[24] and single-bit feedback [9], [25], [26]. DTBF using channel state feedback was demonstrated using UAVs in [27], [28] with feedback required every 50 and 75 ms, respectively. These works validated the feasibility of DTBF using multiple UAVs, but relied on the target to estimate parameters and transmit feedback. Therefore, they cannot be used with a target that is unable to allocate computational or protocol overhead for DTBF.

Feedback can be eliminated by instead relying on beacons transmitted by the target [10]. Although the target must still transmit, it may do so independently, which promotes scalability of the array. In [11], the target broadcasts signals specific for DTBF and requires no intra-array coordination. R-DTBF techniques exploit channel reciprocity between the target and array, and are considered in [6], [18]–[20] for synchronization and beamforming. Arrays that self-synchronize and use indirect relative calibration for R-DTBF are discussed in [12] and demonstrated in [29]. However, this demonstration was carried out in a stationary environment and required nearly 10 seconds to converge. This delay can affect system performance in dynamic environments and could be reduced by improving the speed of frequency synchronization and channel estimation [3]. However, this has not been demonstrated in the literature.

The second type of architecture does not depend on the target transmitting and can beamform to arbitrary directions, enabling applications such as radar and remote sensing. An approach using inter-node range and angle measurements is described in [13], studied with node vibration in [30], and demonstrated in [31]. However, this requires sub-wavelength localization and knowledge of the direction to the target, neither of which are typically available for communications

applications. In [15], an approach that moves an element of the array to be in the direction of the target is developed and demonstrated. Aside from requiring knowledge of the direction to the target, the time to achieve beamforming is constrained by relatively slow movement. Platform rotation has also been shown to increase the beamforming gain [14], but faces a similar issue. Random alignment of unsynchronized carriers is considered in [16] and demonstrated in [32], but this requires repetition coding and reduces the throughput. None of these approaches have been demonstrated in a mobile environment.

Although only a few works report on the channel coherence times for UAVs and DTBF [27], [28], there have been several test campaigns to characterize channels for hovering UAVs. Channel reciprocity error is measured at 900, 1800, and 5000 MHz with a variety of flight conditions in [33]. Hovering displacements are measured and modeled using Gaussian distributions in [34], [35] and bimodal Gaussian distributions in [36]. These offer limited insight into how fast the channel varies, a key design parameter for DTBF systems used in mobile environments.

III. System Model

We consider N UAVs using DTBF for downlink range extension as shown in Fig. 1. The target is assumed to be stationary, unable to provide feedback, and occasionally transmitting standards-compliant bursts for communications with its peers. These bursts are assumed to contain a known preamble and have sufficient power for reception at the UAVs. The UAVs each have a single antenna, transmit and receive on the same radio frequency as the target, and synchronize using intra-network messages independent of the target.

The group of UAVs is divided into one leader and $N-1$ followers so the R-DTBF technique using indirect relative calibration can be applied [12]. The choice of leader is arbitrary and can change with time or be reassigned if one of the UAVs is lost. Since the UAV channels are dominated by a Line-of-Sight (LoS) component [37], we assume that all channels are LoS, linear, and frequency non-selective, but time-varying due to the mobility of the UAVs. The system architecture is shown in Fig. 2.

The following sub-sections describe the underlying approach, effects of time-varying channels, R-DTBF protocol design for fast convergence, and received signal model under the proposed design.

A. Phase Weights for R-DTBF

Transmitter phase weights are to be designed using R-DTBF with indirect relative calibration as described in [12]. The underlying technique is summarized here for completeness. Let $h_{i,j}$ represent the channel between node i and node j, where $i,j \in \{0,1,\ldots,N\}$ and $i \neq j$. Denote node 0 as the target receiver, node 1 as the leader UAV, and nodes $k = \{2,3,\ldots,N\}$ as the follower UAVs. Since the channels are assumed to be frequency flat, $h_{i,j}$ is a single complex coefficient $\alpha_{i,j}e^{j\theta_{i,j}}$ with magnitude $|h_{i,j}| = \alpha_{i,j}$ and phase $\angle h_{i,j} = \theta_{i,j}$. In general, $h_{i,j} \neq h_{j,i}$ due to non-reciprocal transmitter and receiver components, path lengths, and clock

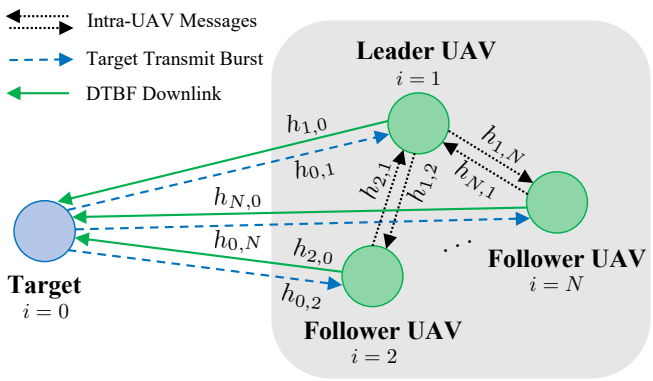

Fig. 2. System architecture for R-DTBF using N UAVs and indirect relative calibration. All links are denoted with scalar channel coefficients $h_{i,j}$.

phases [21]. However, due to reciprocity of the LoS channel, the relative channels are related by [12]

$$\frac{h_{1,0}}{h_{0,1}} = \frac{h_{k,0}}{h_{0,k}}\frac{h_{1,k}}{h_{k,1}}. \tag{1}$$

Based on this relationship, if the leader and followers were to apply the weights

$$w_1 = h_{0,1}^{-1} \tag{2}$$

$$w_k = h_{1,k}(h_{0,k}h_{k,1})^{-1} \tag{3}$$

to their respective transmitted signals, then the channels from all UAVs to the target will be identical

$$w_1 h_{1,0} = w_k h_{k,0} \tag{4}$$

and the signals will coherently combine at the target's receiver. If all UAVs transmit at the same power level, then the phase-only weights

$$w_1 = e^{-j\theta_{0,1}} \tag{5}$$

$$w_k = e^{j(\theta_{1,k}-\theta_{k,1}-\theta_{0,k})} \tag{6}$$

maximize the Signal-to-Noise Ratio (SNR) received by the target, and do not require estimation or inversion of the channel magnitudes [1]. If all nodes are stationary and perfectly synchronized, the channel phases can be modeled as

$$\theta_{i,j} = \phi_{i,T} - 2\pi f_i t_{i,j} + \phi_{j,R} \tag{7}$$

where $\phi_{i,T}$ is node i's transmitter phase, $t_{i,j} = t_{j,i}$ is the propagation delay, f_i is the radio carrier frequency, and $\phi_{j,R}$ is node j's receiver phase. If the leader and followers simultaneously send the symbol m weighted by (5) and (6) respectively, the nominal received symbol at the target will be

$$y = w_1 m e^{j\theta_{1,0}} + \sum_{k=2}^{N} w_k m e^{j\theta_{k,0}} \tag{8}$$

$$= Nme^{j(\phi_{1,T}-\phi_{1,R}-\phi_{0,T}+\phi_{0,R})} \tag{9}$$

where the phase terms unique the followers have all cancelled. In this case, the received symbol power is

$$|y|^2 = N^2|m|^2 \tag{10}$$

which experiences a gain of N^2 due to coherent combining of the N transmitters.

B. Considerations for Time-Varying Channels

In practice, the channel phases will be time-varying due to the mobility of the UAVs and frequency offsets between their unsynchronized oscillators. The corresponding time-varying model for (7) is

$$\theta_{i,j}(t) = (\phi_{i,T} + 2\pi f_i t) - 2\pi f_i t_{i,j}(t) + (\phi_{j,R} - 2\pi f_j t). \quad (11)$$

If $f_i - f_j$ can be accurately estimated and time is maintained by a stable oscillator at all UAVs, then the evolution of the transmitter and receiver phases is predictable, and the only variability is due to the changing path length. This implies that if the phases can be estimated and applied within the coherence time of the channel, i.e., $t_{i,j}(t) \approx t_{i,j}$, then using the modified phase-only weights for the followers

$$\bar{w}_k = e^{j(\theta_{1,k} - \theta_{k,1} - \theta_{0,k})} e^{j2\pi f_{1,k}(-\Delta T_1 + \Delta T_2 + T_{0,k} + \Delta T_3)} \quad (12)$$

will again result in the optimal power gain of N^2 and maximize SNR at the target. In (12), $f_{1,k}$ is the frequency offset of a follower relative to the leader, ΔT_1 is the delay between measurement of $\theta_{1,k}$ and $\theta_{k,1}$, $(\Delta T_2 + T_{0,k})$ is the delay between measurement of $\theta_{1,k}$ and $\theta_{0,k}$, and ΔT_3 is the delay between measurement of $\theta_{1,k}$ and the beamforming transmission using $\bar{w}_k$. The original phase-only weights for the followers (6) have been compensated so they remain phase locked to the leader after their initial measurements of $\theta_{1,k}$.

The challenge therefore becomes periodically estimating the channel phases and synchronization parameters to avoid degradation of the N^2 gain. In order to apply this technique with hovering UAVs, we must understand the channel coherence time and determine the minimum required update rate for the R-DTBF weights (5) (12). We address this in Sec. V and VI, and for now discuss the design of a new R-DTBF protocol for fast synchronization and channel estimation.

C. R-DTBF Protocol Design for Fast Convergence

We propose a time-slotted protocol for R-DTBF similar to [12], [29], but use Gold codes [38] for simultaneous channel access among the UAVs. A similar approach was used for DTBF with receiver feedback in [27], and we extend their work for R-DTBF. The general procedure is described herein and shown in Fig. 3. The leader and followers first exchange sounding waveforms for synchronization and inter-UAV channel estimation. Next is a window for the UAVs to receive a transmission from the target and perform target-to-UAV channel estimation. Finally, the UAVs use the channel phase estimates to transmit a common message using the weights (5) and (12) and form a beam back towards the target. Note that the target is free to transmit at any time. However, to avoid interference with the UAVs, we assume its signal is received within the specified window.

Initialization of the protocol relies on the leader transmitting its sounding waveform. Each follower waits to participate until it has received a sounding waveform from the leader. Once this has occurred, each follower estimates the local time of arrival $\hat{T}_{1,k}$ and frequency offset $\hat{f}_{1,k}$, then schedules its first transmission for the start of the next epoch at $\hat{T}_{1,k} + T_E - \Delta T_1$. After initialization, the protocol steps are as follows:

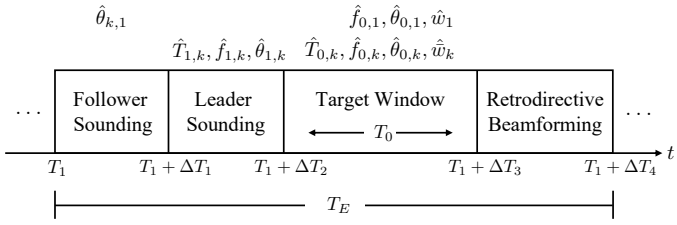

Fig. 3. One epoch of the proposed R-DTBF protocol. Parameters estimated during each segment are shown directly above.

1) The followers simultaneously transmit baseband sounding waveforms $m_k(t)e^{j2\pi \hat{f}_{1,k} t}$ with $m_k(t)$ being binary modulated Gold codes so they can be separated in code space. The leader receives the superposition of these waveforms and estimates each $\hat{\theta}_{k,1}$.
2) The leader transmits $m_1(t)$ at its local time $T_1 + \Delta T_1$, containing its baseband sounding waveform and payload encoding each $\hat{\theta}_{k,1}$. This is received by the followers, which estimate $\hat{T}_{1,k}$ and $\hat{f}_{1,k}$, frequency shift by $-\hat{f}_{1,k}$ to estimate $\hat{\theta}_{1,k}$, and finally decode $\hat{\theta}_{k,1}$.
3) The target transmits $m_0(t)$ consisting of a known preamble and unknown data at time T_0 between $T_1 + \Delta T_2$ and $T_1 + \Delta T_3$. The leader and followers receive this, use the known preamble to estimate the frequency offsets $[\hat{f}_{0,1}, \hat{f}_{0,k}]$, frequency shift by $[-\hat{f}_{0,1}, -\hat{f}_{0,k}]$, and estimate $[\hat{\theta}_{0,1}, \hat{\theta}_{0,k}]$. Additionally, the followers estimate the time of arrival $\hat{T}_{0,k}$ relative to $\hat{T}_{1,k} + \Delta T_2$.
4) At times $T_1 + \Delta T_3$ at the leader and $\hat{T}_{1,k} + \Delta T_3 - \Delta T_1$ at the followers, they transmit a common message $m(t)$ using the estimated R-DTBF weights: $\hat{w}_1 m(t)$ for the leader, and the frequency compensated $\hat{\bar{w}}_k m(t) e^{j2\pi \hat{f}_{1,k} t}$ for the followers.
5) Return to step 1 and repeat.

Since the UAVs synchronize independently of the target, the beamformed signal will have a frequency offset of $-f_{0,1}$. This is assumed to be compensated for by the target during standard demodulation.

Compared to the Time Division Multiple Access (TDMA) protocol used in [29], our proposed protocol has two key modifications. First, motivated by the need for faster convergence, we use Gold codes for Code Division Multiple Access (CDMA). This allows each follower to transmit $N-1$ times longer per epoch, thereby decreasing the overhead, increasing the data available for channel estimation, and reducing the required time for convergence. Second, by reversing the order of the followers and leader, the leader now sends the phase feedback $\hat{\theta}_{k,1}$ within the same epoch instead of after a delay. This allows matching the epoch duration to the channel coherence time and reduces the overhead by a factor of two.

Similar to [29], our proposed protocol is limited to support a fixed number of nodes since the leader must transmit feedback for all followers within $\Delta T_2 - \Delta T_1$. The use of CDMA also requires the followers to be equidistant from the leader or use transmitter power control to avoid the near-far problem. This problem can be easily mitigated by arranging the followers in a circular array around the leader.

D. Received Signal Model for the Proposed Design

A complete model of the received beamformed signal has many terms since errors accumulate as they progress through the protocol steps. However, some of the errors are negligible under typical conditions. For example, distributed transmitters can cause an effect similar to multipath interference due to the distances between them. We assume this delay spread and other timing errors are significantly less than one symbol period so they can safely be ignored. Note that this assumption restricts the size of the array and bandwidth of the signals. For example, a group of UAVs within a 10-by-10 meter grid would have a maximum delay spread of 13.8 ns or one tenth of a symbol at 7.25M symbols/second. The delay spread also causes small phase errors if there are frequency offsets among the UAVs. For the previous example, a 100 Hz frequency error induces a phase error less than one thousandth of a degree due to these terms. Therefore, we assume these errors can also be safely ignored. Finally, we assume unity gain for the transmitter powers and channel magnitudes, as they depend heavily on the choice of hardware, environment, and locations of both the UAVs and target.

With this in mind, the noiseless received signal model for R-DTBF with our proposed protocol design is

$$y_{\text{retro}}(t) = m(t)e^{j\delta\theta_{0,1}} + \sum_{k=2}^{N} m(t)e^{j(2\pi\delta f_{1,k}T_E + \delta\theta_{1,k} + \delta\theta_{k,1} + \delta\theta_{0,k})} \tag{13}$$

where the error terms are prepended with a δ and the delay between follower frequency estimation and beamforming transmission has been set to T_E for simplicity. This in turn assumes that the UAV sounding periods are significantly shorter than the target window and beamforming segment.

For comparison, the equivalent model with feedback from and synchronization to the target is

$$y_{\text{fb}}(t) = \sum_{k=1}^{N} m(t)e^{j(2\pi\delta f_{0,k}T_E + \delta\theta_{0,k})} \tag{14}$$

which involves only one phase error term for each element. In this case, T_E is the delay between the target performing channel estimation and the UAV applying its phase feedback for beamforming.

IV. Error Analysis

The received signal model (13) contains multiple phase errors that affect the beamforming gain. Notable is the term $2\pi\delta f_{1,k}T_E$; if $\delta f_{1,k}$ = 100 Hz as in the previous example, there will be a phase offset of 180° in only 5 ms, leading to destructive interference. In this section, we use simple models for the error terms to gain an understanding of their impact on beamforming performance.

The normalized beamforming gain is

$$G = \left(\frac{|y(t)|}{|y_0(t)|}\right)^2 \tag{15}$$

where $y(t)$ is the received signal model from (13) or (14) and $y_0(t)$ is the same with all error terms set to zero. When the transmitted signals arrive at the receiver with identical power levels, $|y_0(t)|^2 = N^2|m(t)|^2$ is the ideal beamformed power. We are interested in reliable beamforming performance and consider $P(G \geq 0.9)$, the probability that G is at least 90% of its maximum value [13]. First, we set all $\delta f_{0,k}, \delta f_{1,k} = 0$ and assume

$$\delta\theta_{0,1} \text{ and } \delta\theta_{0,k} \sim \mathcal{N}(0, \sigma_\theta^2) \tag{16}$$

$$\delta\theta_{1,k} \text{ and } \delta\theta_{k,1} \sim \mathcal{N}(0, 2\sigma_\theta^2) \tag{17}$$

based on the target being stationary and the phase errors due to UAV hovering, short-term oscillator instability, and receiver noise following a normal distribution. Each UAV is assumed to hover independently of the other UAVs, therefore the phase errors between them have twice the variance in (17). The received signal models (13) and (14) were evaluated using Monte Carlo simulation, and the results are shown in Fig. 4.

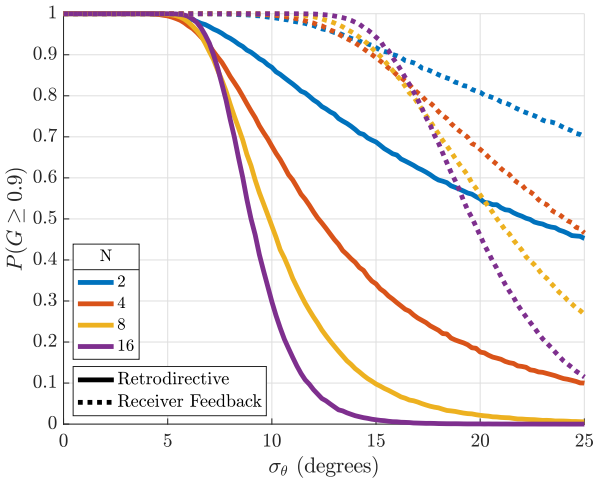

Fig. 4. Probability of the normalized beamforming gain being at least 90% of its maximum with the retrodirective (13) and receiver feedback (14) signal models. N UAVs are considered with no frequency synchronization errors and phase errors modeled by (16) and (17).

These results highlight the sensitivity of the retrodirective technique to phase errors. The additional error terms $\delta\theta_{1,k}, \delta\theta_{k,1}$ between UAVs dominate, and achieving the same performance as the receiver feedback scheme requires a reduction of σ_θ by approximately a factor of two. Achieving $P(G \geq 0.9) \approx 1$ requires $\sigma_\theta \leq 5°$, and there is a sharp drop in performance with N as σ_θ increases. Regarding the feasibility of $\sigma_\theta \leq 5°$, the Cramér-Rao Lower Bound (CRLB) for the phases to be estimated is

$$\sigma_\theta \geq \frac{180}{\pi}\sqrt{\frac{2L-1}{\text{SNR} \times L(L+1)}} \quad \text{degrees} \tag{18}$$

and is attained by the Maximum Likelihood Estimator (MLE) at high SNR or with large data length L [39]. For example, with SNR = 20 dB the MLE achieves $\sigma_\theta = 1.0°$ using $L = 65$ samples. In this regime, the remaining phase error budget of 4.9° can be allocated to UAV hovering, oscillator instability, and other system errors.

Next, we set $\sigma_\theta = 5°$ and assume

$$\delta f_{1,k} \sim \mathcal{N}(0, \sigma_f^2) \tag{19}$$

to evaluate the effects of leader-follower frequency synchronization errors and the protocol delay T_E. The retrodirective model (13) was again evaluated using Monte Carlo simulation, and the results are shown in Fig. 5 for $N = 2$ and $N = 16$ UAVs. These results indicate that exponentially smaller frequency errors are required for longer protocol delays, and as in Fig. 4, the likelihood of achieving $G \geq 0.9$ decreases with N. For example, consider $T_E = 100$ ms, which requires $\sigma_f \leq 0.3$ Hz for $P(G \geq 0.9) \approx 1$ from Fig. 5. The CRLB for a follower estimating the frequency offset is

$$\sigma_f \geq F_s \sqrt{\frac{6}{\text{SNR} \times (2\pi)^2 L(L^2-1)}} \quad \text{Hz} \qquad (20)$$

and is attained by the MLE at high SNR or large L [39]. Continuing the example with SNR $= 20$ dB, the MLE achieves $\sigma_f = 0.3$ Hz for a sample rate of $F_s = 250$K samples/second and $L = 1019$ samples, over 15 times the amount of data required for $\sigma_\theta = 1°$. For situations where it is not possible to obtain large L from a single measurement, M measurements using smaller L can be averaged to reduce the variance by a factor of M. Alternatively, Kalman filters that utilize successive phase estimates can be used for accurate frequency estimation [40], [41].

From this analysis, it is clear that (i) the UAVs should generate their carrier frequencies using stable and accurate references, and (ii) compensating for any frequency offsets between the UAVs will dominate the time required to achieve $G \geq 0.9$. As N increases, TDMA protocols similar to the one used in [29] will reduce the number of samples per element and require additional time for convergence. Conversely, the CDMA protocol proposed in Sec. III-C keeps the number of samples per element constant regardless of N. The two protocols were compared using simulation of the MLE and averaging multiple estimates over time. We set $T_E = 100$ ms, L to 25% of a slot, SNR$=$ 20 dB, $F_s = 250K$ samples/second, and required $\sigma_f \leq 0.3$ Hz. The results in Fig. 6 show the convergence time in each case. The proposed CDMA protocol requires constant time, while the time required for the TDMA protocol of [29] increases exponentially with N. This is expected, since (20) depends on L^3 and L decreases linearly with N.

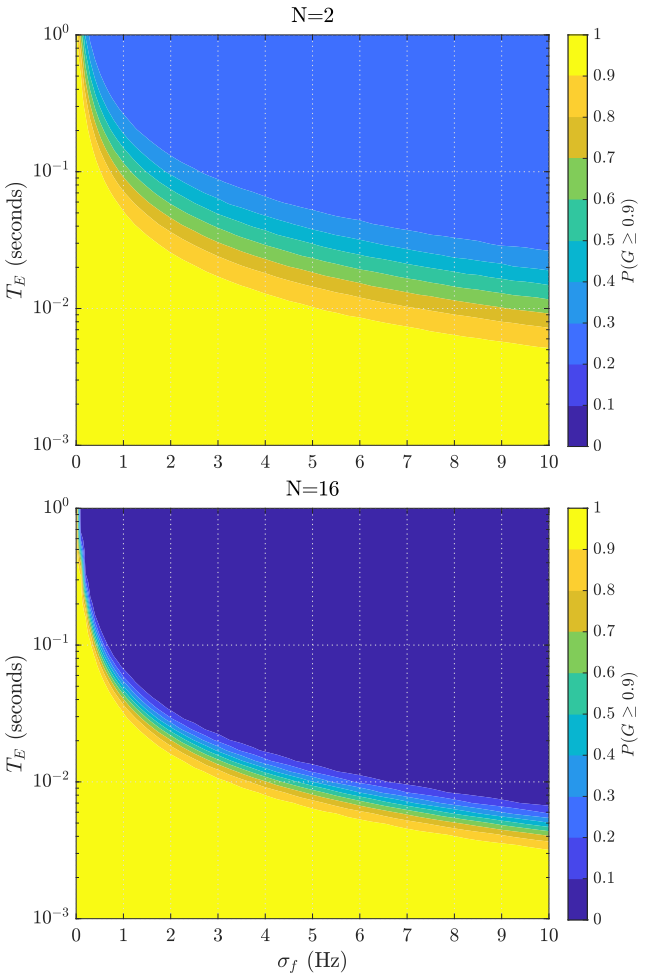

Fig. 5. Probability of the normalized beamforming gain being at least 90% of its maximum with frequency errors modeled by (19), phase errors modeled by (16) and (17) with $\sigma_\theta = 5°$, and $N = 2$ (top) or $N = 16$ (bottom) UAVs.

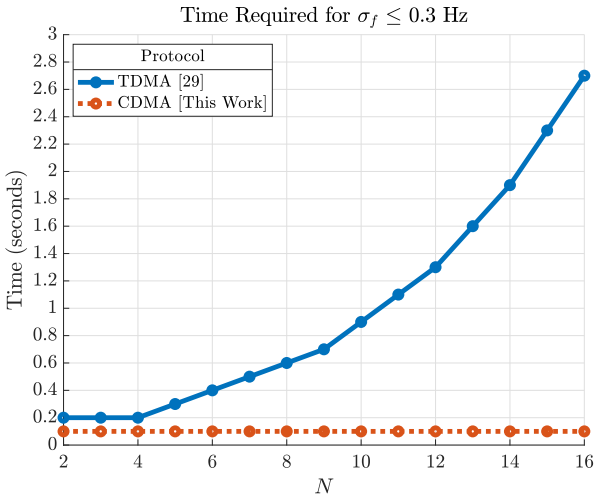

Fig. 6. Comparison of the time required for $\sigma_f \leq 0.3$ Hz using N UAVs and the TDMA protocol from [29] or the CDMA protocol from Sec. III-C.

V. Channel Phase Modeling

Sec. IV bounded the phase errors for reliable beamforming performance and showed that estimation errors would be insignificant with high SNR. In this section, we use experiments to develop simple models of the phase errors due to UAV hovering and short-term oscillator stability in three frequency bands: 915, 2550, and 5900 MHz. The following sub-sections describe the data collection, processing, and resulting models for both types of phase errors. The models are applied in Sec. VI to evaluate R-DTBF performance with UAVs.

A. UAV Hovering

Small-scale movements from a UAV hovering about its ideal location cause channel phase variations and pose a challenge for R-DTBF. Because of this, the phase estimates obtained at T_1 may not be useful for beamforming after a delay of ΔT_3. Ideally, $T_E \leq T_C$ where T_C is the channel coherence time, the duration for which the channel phase changes by less than

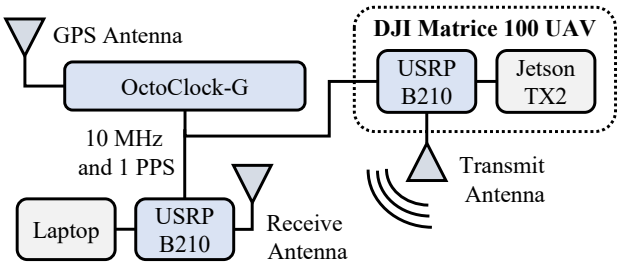

Fig. 7. Block diagram of the test setup for collecting channel phase measurements for a hovering UAV. The UAV transmitter and ground receiver were synchronized by running long cables to an OctoClock-G.

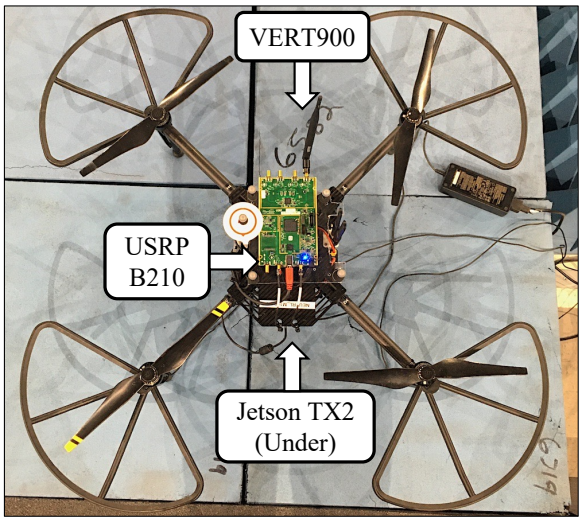

Fig. 8. DJI Matrice 100 UAV equipped with the Jetston TX2 processor, B210 SDR, and VERT900 antenna for channel phase measurements at 915 MHz.

a specified tolerance. Based on the results of Sec. IV, we are interested in setting $T_E \leq T_C$ such that $\sigma_\theta \leq 5°$. Hovering characteristics are likely to differ between classes of UAVs and are complex to model. Instead, we turn to measurements to develop a statistical model of the hovering phase variations for a given type of UAV. Although this is specific to a single UAV and its flight conditions, it lends insights into what may be expected for similar UAVs. Additionally, the framework and processing methodology can be reused for other platforms.

Previous works have measured UAV hovering characteristics using real-time kinematic GPS and inertial sensors [34]–[36] or radio channel sounding [33]. Our objective was to characterize the phase variations due to a UAV hovering in an ideal environment and without synchronization errors. Therefore, we conducted radio channel sounding measurements inside of an anechoic chamber and with all radios synchronized to a common clock. The experiment setup and UAV platform used are shown in Figs. 7 and 8, respectively. We used the DJI Matrice 100 equipped with an NVIDIA Jetson TX2 processor and Ettus Research B210 SDR as a transmitter. The ground receiver used a separate B210 SDR and collected raw in-phase and quadrature (IQ) samples at a rate of 1M samples/second onto a laptop. Long cables were used to distribute the 10 MHz and 1 pulse-per-second (PPS) frequency and time references from an OctoClock-G to both SDRs.

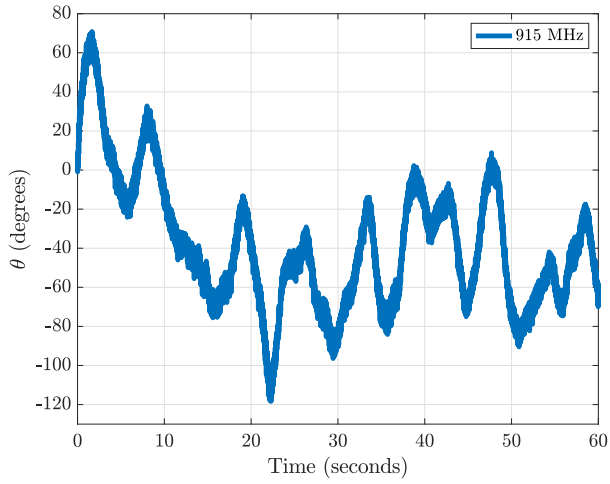

Fig. 9. Example phase trajectory for the UAV hovering while transmitting at 915 MHz. The samples were decimated by a factor of 5000 for plotting.

A typical measurement involved the UAV hovering for 60 to 90 seconds at a distance of 7 m and altitude of 2.5 m relative to the stationary ground receiver. The positions of the UAV and ground receiver were continuously recorded using an OptiTrack system for post-processing. The UAV transmitted a complex baseband tone at 10 kHz modulated onto a carrier frequency of 915, 2550, or 5900 MHz. These frequencies were chosen to avoid interference with the DJI remote control and a Wi-Fi router. The UAV transmitter and ground receiver both used Ettus Research VERT900 and VERT2450 antennas for coverage of the three frequency bands. The ground receiver was configured for maximum gain, and the UAV transmitter power was set such that the power of the received IQ samples was approximately 10 dB below full scale.

The received IQ samples were pre-processed by isolating segments where the UAV was hovering based on the OptiTrack data. Frequency-domain analysis revealed Doppler spreads up to +/- 4 kHz during the experiments. Therefore, a filter passing 6-14 kHz was applied to the raw data. Instantaneous phases relative to the ideal 10 kHz tone were estimated to produce channel phase measurements every 1 μs. The relative phase estimates were unwrapped to remove discontinuities at $\pm\pi$, yielding a phase trajectory θ. An example trajectory over one minute is shown in Fig. 9. It can be seen that θ varies by about 190°, with shorter term variations of 10° to 20°.

Next, each trajectory was processed using a sliding window of duration T_W. Within this window, the difference between the initial and final phases $\theta_D = \theta_{\text{final}} - \theta_{\text{init}}$ was computed and saved. The window then slid forward in time by one sample and the process was repeated. This was carried out for each of the data sets with T_W ranging from 100 μs to 1 s. The collection of θ_D for each T_W and frequency were then fit to normal distributions $\theta_D \sim \mathcal{N}(0, \sigma^2_{\theta_D})$. Sample distributions of the measured data and model fits are shown in Fig. 10. The measurement distributions were skewed or bimodal at times, highlighting the error under this modeling assumption. Despite this, we continued with the normal distribution for simplicity. The effect of this assumption is evaluated in Sec. VI.

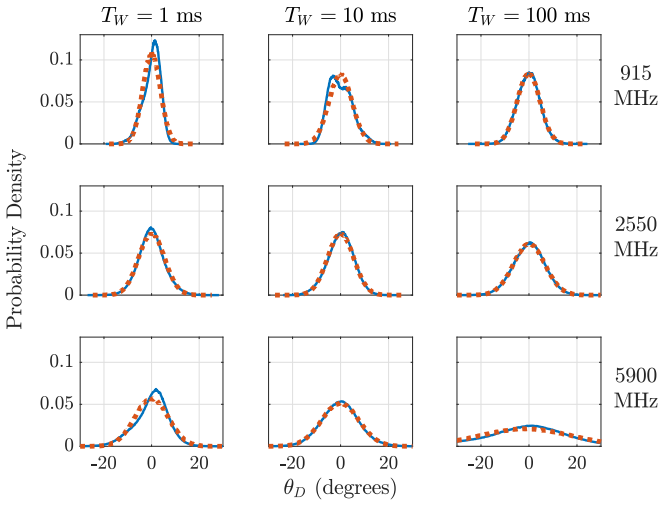

Fig. 10. Samples of the measured data distributions (solid) and models fit (dashed) for the channel phase differences due to a UAV hovering using three center frequencies (rows) and time window durations (columns).

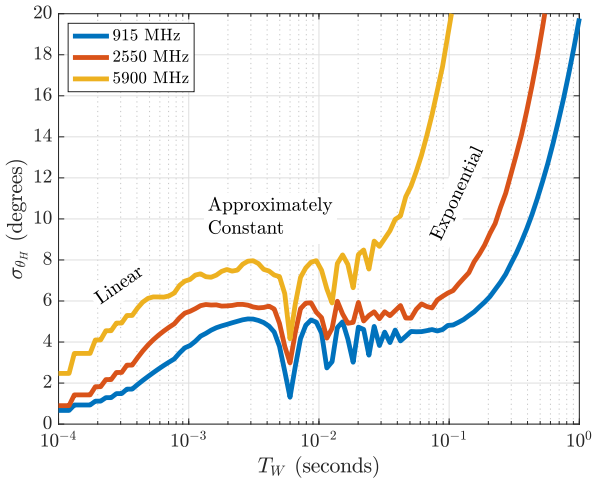

Fig. 12. Standard deviation of normal distribution models fit for the channel phase differences over different time durations due to UAV hovering.

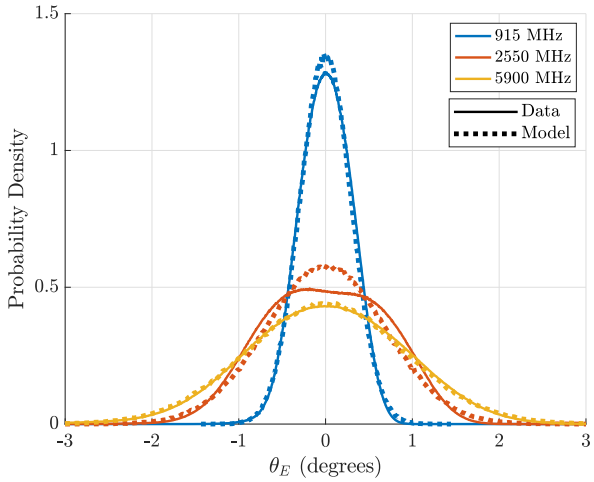

Fig. 11. Distributions of the measured data and models for channel phase errors due to noise and imperfect synchronization between two B210 SDRs receiving reference clocks from the same OctoClock-G.

Since the received SNR was approximately 50 dB during all measurements, the estimation errors were negligible. However, the two SDRs were not perfectly synchronized due to the independent phase noises of their local oscillators. These errors were characterized by a separate set of measurements through a wired channel and modeled as $\theta_E \sim \mathcal{N}(0, \sigma^2_{\theta_E})$ where $\sigma_{\theta_E} = [0.3°, 0.7°, 0.9°]$ for [915, 2250, 5900] MHz. A comparison between the distribution of the measurements and this model is shown in Fig. 11. Once again, we observed that the normal models were a reasonably good fit.

Assuming independent errors θ_E when estimating the phase differences θ_D, the phase errors due to hovering were modeled as $\theta_H \sim \mathcal{N}(0, \sigma^2_{\theta_H})$ where

$$\sigma_{\theta_H} = \sqrt{\sigma^2_{\theta_D} - \sigma^2_{\theta_E}}. \tag{21}$$

The models for each carrier frequency and window duration are shown in Fig. 12. The trends agreed with intuition, as the hovering phase errors increased with carrier frequency and window duration. Analysis of the phase trajectories revealed an oscillation with a period of 6 ms when the UAV's propellers rotated at flight speeds. Therefore, matching T_W to the propeller rotation period or one of its harmonics should result in lower values of σ_{θ_H}. This can be clearly seen in Fig. 12. Three regimes were observed:

1) σ_{θ_H} increased linearly while T_W was less than the propeller rotation period.
2) σ_{θ_H} was minimized when T_W^{-1} was matched to a harmonic of the propeller rotation frequency, but was otherwise approximately constant.
3) σ_{θ_H} increased exponentially with T_W due to larger-scale movements of the UAV.

B. Short-Term Oscillator Stability

Next, we considered the short-term time-varying behavior of the independent local oscillators used by the UAV radios. Oscillator instabilities induce errors in the phase estimates and reduce the achievable beamforming gain. These errors can be managed by choosing a sufficiently stable oscillator; for example, the demonstrations in [22], [29] utilized oven-controlled crystal oscillators (OCXOs). We sought to understand the phase errors using three types of oscillators typically paired with the B210 SDRs: the onboard 40 MHz crystal oscillator (Internal), the Jackson Labs LC_XO 10 MHz temperature compensated crystal oscillator (TCXO), and the OCXO version of the LC_XO. To this end, we conducted additional measurements to develop statistical models of the short-term phase errors for each type of oscillator.

The test setup consisted of two B210s connected via a wired channel with each synchronized to an independent and identical frequency reference. The LC_XOs were operated without GPS and the equipment was allowed to warm up for 30 minutes before each measurement. The data collection and processing followed Sec. V-A, except the average frequency

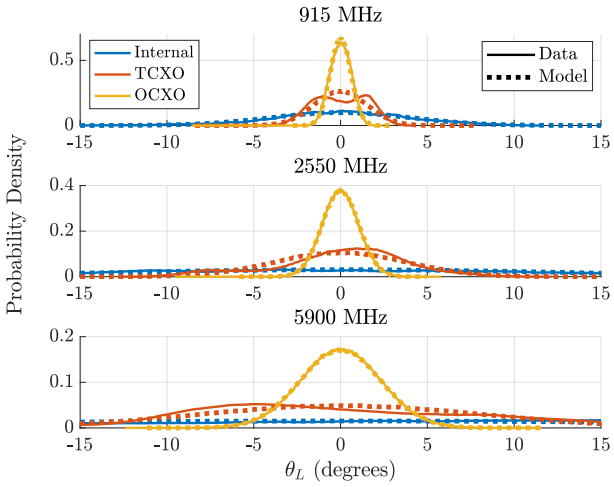

Fig. 13. Sample distributions of the measured data and models for phase errors over $T_W = 10$ ms using three oscillators and carrier frequencies.

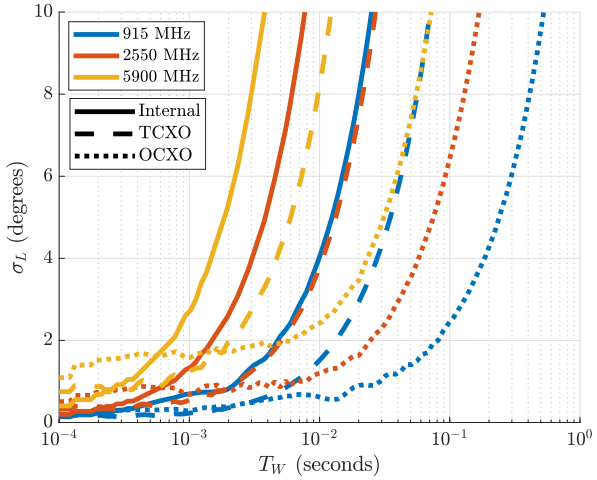

Fig. 14. Standard deviation of normal distribution models fit for the channel phase differences due to instabilities between independent oscillators.

offset was estimated and removed between bandpass filtering and relative phase estimation. This produced sets of phase differences θ_L for each of the oscillators and carrier frequencies. Each was fit to a normal distribution $\theta_L \sim \mathcal{N}(0, \sigma^2_{\theta_L})$ with a sample comparison between the data and model shown in Fig. 13 and the set of all σ_{θ_L} versus T_W in Fig. 14.

As shown in Fig. 13, the distributions of the measured data were skewed or bimodal at times. The normal distribution fit was again used for simplicity at the expense of modeling error. The general trends observed in Fig. 13 and 14 agreed with expectations: the internal oscillator has the most variation, the TCXO option has improved stability, and the OCXO option offers the most stability. It was interesting to observe that for window durations of less than 1 ms the OCXO had the largest phase variability. We note that its data sheet indicates a higher level of phase noise for offsets ≥ 10 kHz from the carrier as compared to the TCXO and internal oscillators [42]–[44].

TABLE I
MAXIMUM R-DTBF PROTOCOL DURATIONS (IN MILLISECONDS) WITH $N = 4$ INDEPENDENTLY HOVERING UAVS

	915 MHz	**2550 MHz**	**5900 MHz**
Internal	6.5	0.5	0.2
TCXO	18	6	0.2
OCXO	43	12	6

VI. EXPECTED PERFORMANCE WITH UAVS

The analysis from Sec. IV is now revisited using the data and models experimentally derived in Sec. V. Instead of varying the standard deviation of phase errors, we now vary the R-DTBF protocol duration T_E to determine the required duration for $G \geq 0.9$ with high probability. We compare the combined phase errors from the models of θ_H and θ_L to those drawn from the measured samples using Monte Carlo simulation. The number of UAVs was $N = 4$ and each was assumed to hover independently. The followers' frequency errors were modeled using (19) with $\sigma_f = 0.3$ Hz. The normalized beamforming gain G was evaluated for the R-DTBF received signal model (13) with $T_E = T_W$.

Simulations were conducted for all carrier frequencies and oscillator options from Sec. V, and the results are shown in Fig. 15. The results indicate a good agreement between the models and samples from the measured data, with an error less than 1% on average. Effects from propeller rotation can be seen and are most notable at 5900 MHz. Interestingly, this effect is not observed when using the internal oscillator. This is because it is the dominant source of phase errors, and G is less likely to reach 90%. It is also interesting to observe that the fall-off from $P(G \geq 0.9) \approx 1$ is slightly more gradual at the higher frequencies.

The resulting maximum R-DTBF protocol durations for $P(G \geq 0.9) \approx 1$ are summarized in Table I. These results yield insight into the required update rates and oscillator stability to realize R-DTBF using UAVs. These requirements can add to the system cost and mandate significant overhead due to the frequency of UAV sounding for timely phase updates. Given the bandwidth limitations discussed in Sec. III, using the internal oscillator at [2550, 5900] MHz or TCXO at 5900 MHz are unlikely to find practical use due to the required update periods of 0.5 and 0.2 ms, respectively. In these cases, there is little time that can be allocated for the target to transmit with a low probability of collision. The other configurations are of interest if the SNR is high, since short duration sounding waveforms can be used with negligible estimation errors (as discussed in Sec. IV). High SNRs can be achieved by flying the UAVs relatively close together and operating with target radios that emit at high power levels or with sufficiently long preambles.

We emphasize that these results are based on measurements and models of the phase variations from hovering inside of an anechoic chamber under close to ideal conditions. In practice, the UAVs may be affected by wind and other factors, and reliable beamforming may require even faster update rates.

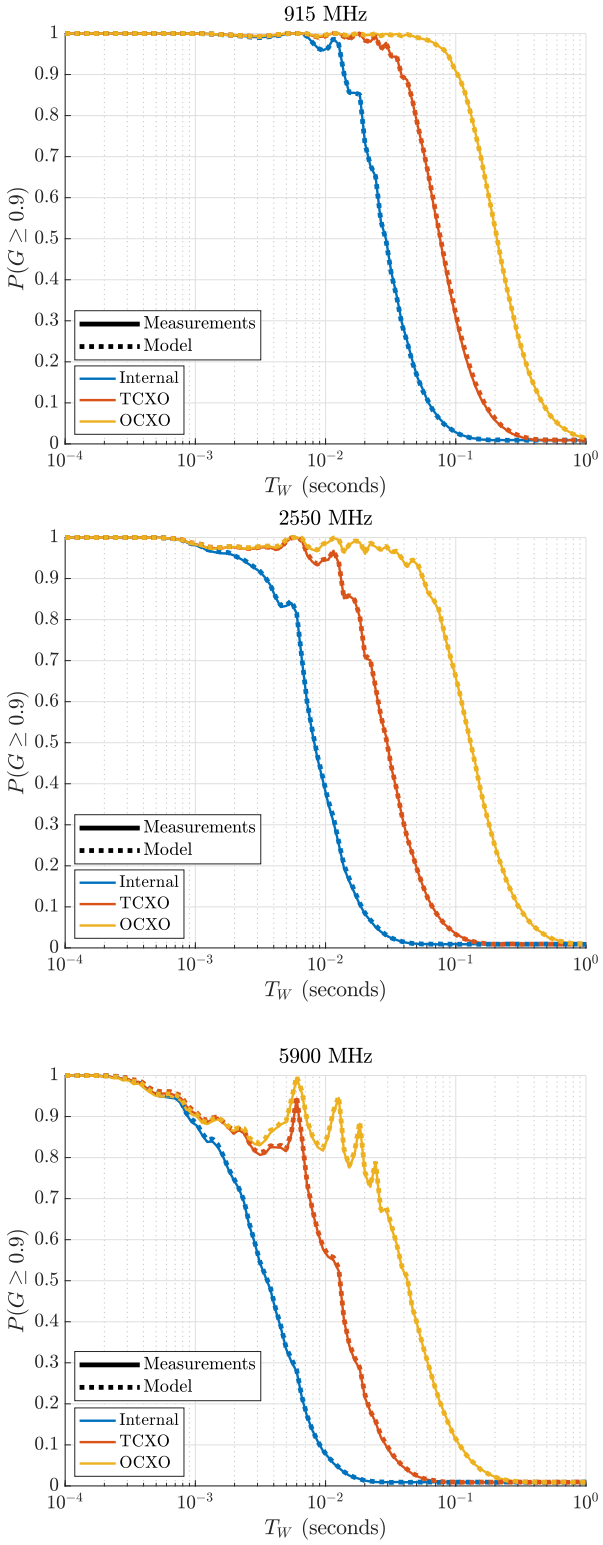

Fig. 15. Probability of the normalized beamforming gain being at least 90% with $N = 4$ UAVs, frequency errors modeled by (19) with $\sigma_f = 0.3$ Hz, and R-DTBF weights updated every T_W seconds. Shown for carrier frequencies of 915 (top), 2550 (middle), and 5900 (bottom) MHz with three types of oscillators (Internal, TCXO, OCXO). The solid lines are based on samples drawn from the measured data from Sec. V, while the dotted lines are based on samples drawn from the models fit using normal distributions.

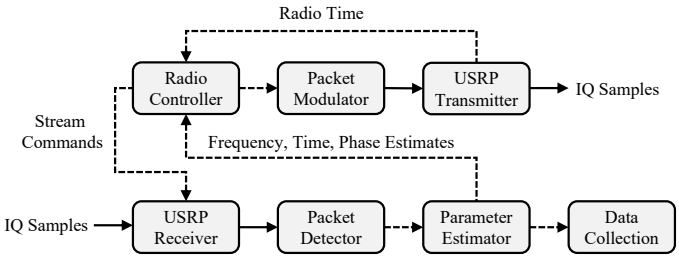

Fig. 16. Block diagram of the GNU Radio software processing for each node. Solid lines denote streams of IQ samples and dashed lines denote metadata or packetized IQ samples with metadata.

VII. Experimental Validation

The results of Sec. VI predict that certain configurations of the R-DTBF system using UAVs were feasible to demonstrate under nominal conditions. We further investigated this using rapid prototyping and a set of preliminary experiments. Our goals were to first evaluate the performance in a laboratory setting and then transition the implementation to testing with UAVs. Our experimental validations were limited to three nodes for the initial proof-of-concept. The following subsections describe the details of the implementation, the level of synchronization achieved between a leader and two followers, and the first results of R-DTBF in a mobile environment.

A. Implementation Details

Each node was equipped with a laptop computer, USRP B210 SDR, LC_XO OCXO, and VERT900 antenna. The LC_XOs were used without GPS lock, so each node had an independent 10 MHz reference to derive its clock and carrier frequencies. All nodes used a carrier frequency of 915 MHz and Binary Phase Shift Key (BPSK) modulation at a rate of 250K symbols/second. The leader/follower sounding and target transmit waveforms consisted of 250 bits (1 ms duration) of a unique Gold code generated by the node's identifier $i \in \{0, 1, 2, 3\}$. The R-DTBF protocol epoch duration was $T_E = 100$ ms with $\Delta T_1 = 25$ ms, $\Delta T_2 = 50$ ms, and $\Delta T_3 = 75$ ms. The choice of $T_E = 100$ ms was due to software processing constraints, and predicted losses will be noted where applicable.

The transmitter and receiver processing was implemented using the GNU Radio software development toolkit. A block diagram of the signal-flow graph is shown in Fig. 16. The radio controller maintained protocol timing, informed the modulator of the required frequency and phase shifts for R-DTBF, encoded phase feedback for the leader to send to the followers, and scheduled all transmit and receive operations. The receiver first applied power detection to identify packets of IQ samples for parameter estimation. The packet's power, frequency offset, time of arrival, and phase offset were then estimated and sent to the radio controller. Data including the raw IQ samples and parameter estimates were collected for post-processing. Note that while this architecture was common for all nodes, the target did not adapt its transmitter in any way, and its receiver was configured solely for data collection.

The bulk of the processing was implemented in the parameter estimators of the leader and follower nodes. First, a bank of matched filters with copies of the modulated Gold codes for each node was used to detect which nodes were on the channel and estimate their power levels. Next, the frequency offset was estimated if the packet was from the leader or target. This was done by squaring the received BPSK signal to create a tone at twice the carrier offset. The frequency of this tone was estimated using a Fast Fourier Transform (FFT) and averaged using up to 100 estimates (10 seconds) for each node.

After the frequency offset was removed, the samples were again processed using the bank of matched filters to estimate the relative time of arrival and phase offset for each waveform detected. Samples around the peak power out of the matched filters were interpolated to obtain fine estimates of the timing and phase. If the waveform was from the leader, these estimates were then used to demodulate and decode the phase feedback $\hat{\theta}_{k,1}$ at each of the followers. The leader encoded each $\hat{\theta}_{k,1}$ using 16 bits and appended all phases to the end of its Gold code prior to BPSK modulation.

As described in Sec. III, the followers first received an entire epoch to locate the leader's sounding waveform and schedule their future transmit and receive operations. After each receive operation, the parameter estimates were sent to the radio controller within 5 ms to prepare for synchronization and beamforming during the same epoch.

B. Leader/Follower Synchronization

The first experiment was designed to evaluate the frequency and phase synchronization of the followers relative to the leader. The setup is shown in Fig. 17 and consisted of one leader and two followers with the antennas stationary and separated by about 3 m. The leader transmitted its sounding waveform every $T_E = 100$ ms, and the followers estimated the frequency offsets $\hat{f}_{1,k}$ and phases $\hat{\theta}_{1,k}$. The followers then both simultaneously transmitted $\Delta T_3 = 75$ ms after the leader with upconversion by $\hat{f}_{1,k}$ and a phase rotation of $e^{j\hat{\theta}_{1,k}}$. Though not part of the R-DTBF protocol, the purpose of this phase rotation was so that the followers' signals would each arrive with a constant phase at the leader when they had correctly accounted for their frequency offsets.

Frequency offsets estimated at each of the followers over a period of 80 seconds are shown in Fig. 18. These are compared to their true values, which were independently measured to a resolution of 0.1 Hz using a spectrum analyzer. The initial effect of the moving average can be seen, and after the first ten seconds the errors had means $\mu_f = [0.06, 0.18]$ Hz and standard deviations $\sigma_f = [0.10, 0.14]$ Hz. Based on the analysis in Sec. IV, this level of frequency synchronization is sufficient for obtaining $G \geq 0.9$ with high probability.

During the same test, the leader estimated the received phase for each of the followers' waveforms. The results are shown in Fig. 19, and the standard deviation of the received phases were 2.3° and 2.6° for the two followers. According to the results of Sec. IV, these are also sufficient for obtaining $G \geq 0.9$ with high probability. Further, they are in close agreement with the oscillator measurements when $T_W = 100$ ms in Fig. 14.

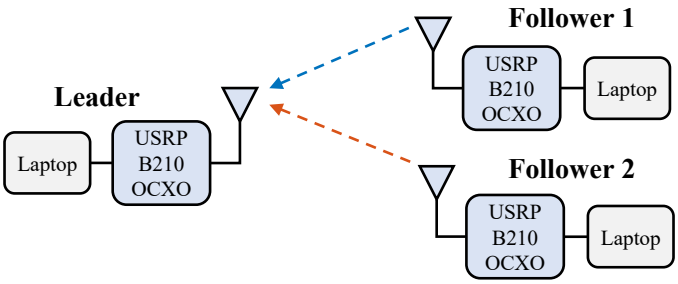

Fig. 17. Block diagram of the test setup for evaluating synchronization between the leader and two followers. All nodes used independent clocks, and their antennas were separated by about 3 m.

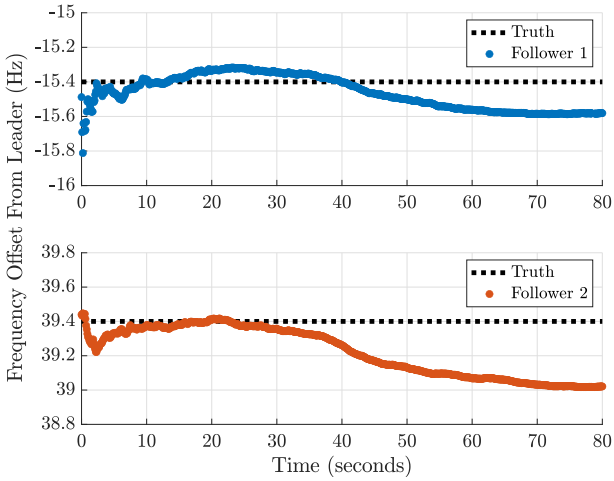

Fig. 18. Frequency offset of the leader estimated at the followers. The estimates were immediately within 1 Hz of the true value.

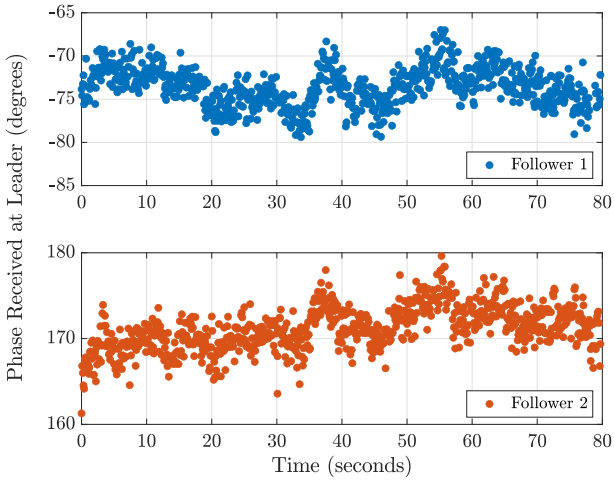

Fig. 19. Phase of arrival for the two follower waveforms simultaneously received at and estimated by the leader.

These results demonstrated that sufficient synchronization can be achieved for reliable beamforming performance with two followers and one leader. Further, we demonstrated the use of Gold codes for the two followers transmitting to the leader simultaneously. Next, we build from these results with a more complete demonstration of R-DTBF.

C. R-DTBF with Handheld Antennas

The test setup from Sec. VII-B was reconfigured to have one leader, one follower, and one target as shown in Fig. 20. The leader received its time and frequency references from an OctoClock-G that shared its 1 PPS signal with the target. The purpose of this arrangement was to have the target transmit at a fixed offset from $\Delta T_3 = 75$ ms within each epoch.

The leader and follower used long cables to handheld antennas. Channel phase measurements were first collected with the follower temporarily using the same OCXO reference as the leader. Measurements were taken while each antenna was held about 2 m apart while walking in place. Processing these measurements using the approach from Sec. V resulted in phase errors with $\sigma_{\theta_H} = 5.6°$, similar to several of the UAV hovering models from Fig. 12. Along with the OCXO errors from Fig. 14, $\sigma_f = 0.14$ Hz from the previous test, and $T_W = 100$ ms, we predicted $P(G \geq 0.9) = 0.97$ for this test.

The follower was then returned to its own OCXO, and an R-DTBF experiment was conducted with 5 seconds of setup and 30 seconds of walking in place. The target receiver was stationary and about 3 m away from both handheld antennas. The target collected received power levels for each step of the R-DTBF protocol, and the results over time are shown in Fig. 21. This figure compares the individual powers of the leader and follower, actual power achieved during beamforming, and the optimal beamformed power based on the individual power levels. We observed that the actual beamformed power levels were within 2 dB of optimal in 200 ms, and they closely tracked theory throughout the experiment.

An example of the received BPSK signals with and without beamforming is shown in Fig. 22. This example was taken from about 3 seconds into the experiment, when the power levels received from the leader and follower were approximately equal. For this particular measurement, we observed $G = 0.98$. The unshaded portion of Fig. 21 denotes the 30 second test period when both antennas were handheld with walking in place. During this period, we observed $P(G \geq 0.9) = 0.92$, a 5% difference from our prediction. This difference is likely due to system errors not captured by our model, such as the minor biases in the frequency offset estimates, and implementation errors, such as the notable outliers caused by one of the B210s occasionally failing to transmit on time.

These results demonstrated a close agreement between our predictions and actual performance. Unlike the R-DTBF results from [29], our results converged almost instantly and tracked a time-varying channel. Additionally, this experiment used phase errors representative of those observed for a UAV hovering. The results supported the feasibility of the concept and reduced risk for our subsequent demonstration with UAVs.

D. R-DTBF with UAVs

The implementation was next evaluated using hovering UAVs for the leader and follower. The test setup was similar to Fig. 20, but the leader and follower used VERT900 antennas mounted on DJI Matrice 100 UAVs with long cables to the B210s. The B210s were connected to a single desktop computer for processing, but there was no synchronization of

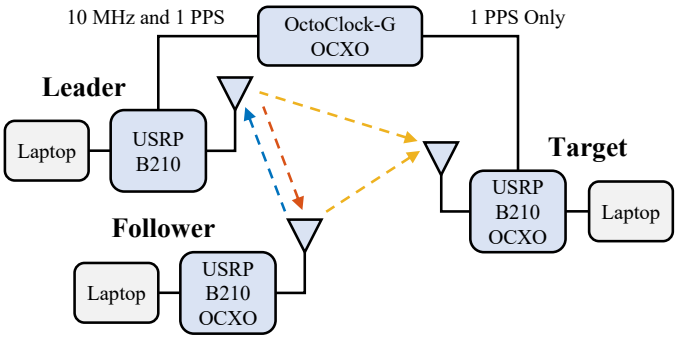

Fig. 20. Block diagram of the test setup for R-DTBF with handheld antennas. The leader and target shared a 1 PPS reference to support triggered collection of the received signal powers with respect to the leader's clock.

Fig. 21. Power levels received by the target and compared to optimal beamforming during the R-DTBF experiment with handheld antennas. All power levels are shown in dB relative to full scale (dBFS).

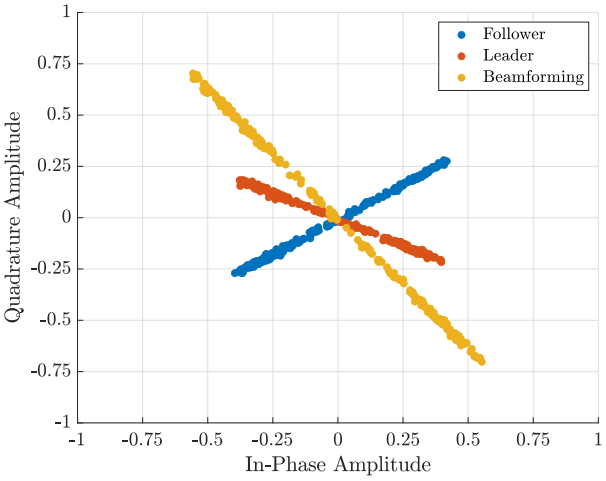

Fig. 22. Example of the received BPSK constellations at the target during one epoch of the R-DTBF protocol. The beamformed signal has approximately twice the amplitude (four times the power) of the individual signals from the leader and follower.

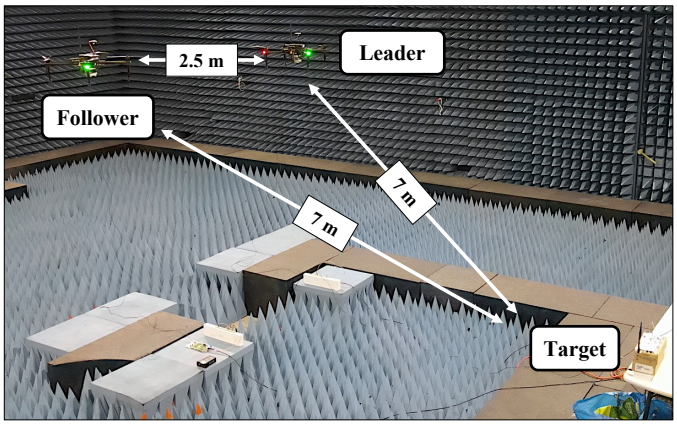

Fig. 23. Test setup for R-DTBF using two DJI Matrice 100 UAVs.

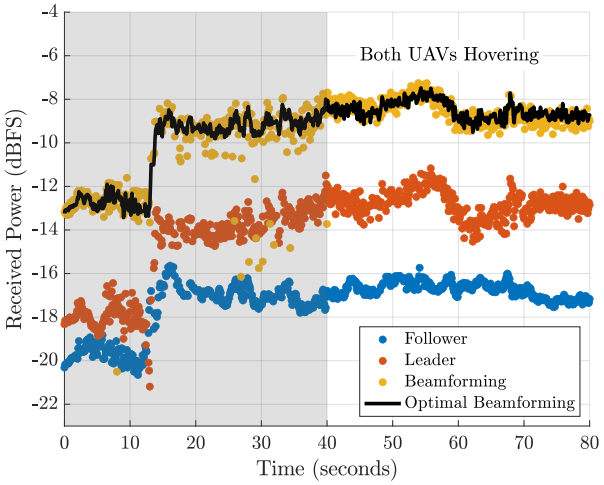

Fig. 24. Power levels received by the target and compared to optimal beamforming during the R-DTBF experiment with UAVs.

any kind between the computer and B210s. Each B210 used an independent 10 MHz reference from its OCXO. The leader and follower used independent 1 PPS references as previously described. This configuration allowed us to rapidly test the performance of R-DTBF without optimizing the software for the Jetson TX2 processors onboard the UAVs.

The experiment involved the leader and follower UAVs hovering at an altitude of 2.5 m with distances of 2.5 m between them and 7 m to the target inside of an anechoic chamber. This setup is shown in Fig. 23. The UAVs were observed to hover independently with this separation, as desired to predict performance using the channel model from Sec. V. The UAV transmitter power levels were set so the received power levels would be similar to those used during the handheld experiment. Each UAV was flown manually by an independent operator. Once airborne, the positions of the UAVs were first adjusted to achieve the separations previously described. Next, the operators attempted to keep the UAVs hovering in their desired positions for at least 30 seconds. Based on the UAV hovering and OCXO phase error models for 915 MHz, $\sigma_f = 0.14$ Hz, and sub-optimal choice of $T_W = 100$ ms for our software implementation, we again predicted $P(G \geq 0.9) = 0.97$ for this test.

The results of the experiment are shown in Fig. 24. Both UAVs took-off at around 15 seconds, had their positions adjusted until 40 seconds, and then hovered until 80 seconds. We again observed that the results converged almost instantly and tracked optimal performance for the duration of the experiment. The unshaded region shows where both UAVs were hovering as desired. We observed $P(G \geq 0.9) = 0.87$ during this period, a 10% difference from expected. In addition to the reasons previously described, this difference was also attributed to the larger power spread of the leader compared to the handheld experiment. The leader's transmitted power was not consistent between bursts, which led to results that both exceeded and fell short of $G = 1$ by up to 20% (0.8 dB for the power levels used) an almost equal number of times. We note that $E[G] = 0.99$ over this same period. The cause of this power spread was later identified to be an artifact of the B210 transmitter used by the leader.

VIII. Discussion

The R-DTBF results with two hovering UAVs in Sec. VII-D had an error of 10% compared to our modeling predictions. This was an additional 5% difference compared to the handheld measurements in Sec. VII-C. The results were reasonably accurate compared to our predictions, with some of the differences briefly discussed in each of the respective sections. In this section, we discuss other sources of errors and considerations for practical use cases.

Errors between the modeling predictions and measured performance can arise for several reasons. While we have not isolated the exact causes, we have identified the most probable ones. First, the model assumed that all UAVs hovered independently and identically. This assumption will not hold when the UAVs are in close proximity since drafts from the propellers of one UAV will cause displacements to nearby UAVs. It would also not hold if the UAVs had notable differences, for example if a propeller is slightly damaged or if an antenna is not attached securely. Second, with two or more UAVs there will be additional time-varying multipath components from the airframes and propellers that were not captured by the single UAV model. The additional multipath may cause the channel phase differences to be larger than reported in Fig. 12. While we attempted to mitigate the first of these effects with sufficient UAV spacing during our experiments, the second was unaccounted for.

As discussed in Sec. VI, our modeling was based on a single UAV hovering inside of an anechoic chamber under close to ideal conditions. These conditions were selected to provide a simple and inexpensive starting point for validating the feasibility and performance of R-DTBF using hovering UAVs. In practice, the hovering of the UAVs may be affected by wind, and the system range may be reduced due to multipath fading. Different environments and UAV stabilization capabilities should be considered when optimizing the system design, and will be the subject of future work.

IX. Conclusion

This paper validated the feasibility of a wireless communications system using R-DTBF from a group of hovering UAVs for downlink range extension. The architecture enables the use of multiple small UAVs instead of one large and expensive UAV that has a single point of failure. Further, it does not rely on feedback from the target receiver or position information, promoting scalability of the distributed array. We proposed an R-DTBF protocol using Gold codes for simultaneous channel sounding and fast convergence, developed the received signal model, and analyzed the key error terms. We used measurement campaigns to derive statistical models of the channel phase variations due to a UAV hovering at 915, 2550, and 5900 MHz. Beamforming performance was predicted under these models and experimentally validated using two DJI M100 UAVs. To the best of our knowledge, these were the first demonstrations of DTBF without feedback in a mobile environment. We observed convergence in 200 ms with beamforming gains over 90% of the theoretical maximum and within 10% of our modeling predictions. As part of our future work, we plan to demonstrate the system in an outdoor environment using additional UAVs.

Acknowledgments

The authors acknowledge the Office of Naval Research, Naval Research Laboratory, United States Air Force, and MIT Lincoln Laboratory for supporting this research.

References

[1] R. Mudumbai, D. R. Brown III, U. Madhow and H. V. Poor, "Distributed transmit beamforming: challenges and recent progress," in *IEEE Communications Magazine*, vol. 47, no. 2, pp. 102-110, February 2009.

[2] S. Jayaprakasam, S. K. A. Rahim and C. Y. Leow, "Distributed and Collaborative Beamforming in Wireless Sensor Networks: Classifications, Trends, and Research Directions," in *IEEE Communications Surveys & Tutorials*, vol. 19, no. 4, pp. 2092-2116, Fourthquarter 2017.

[3] J. A. Nanzer, S. R. Mghabghab, S. M. Ellison and A. Schlegel, "Distributed Phased Arrays: Challenges and Recent Advances," in *IEEE Transactions on Microwave Theory and Techniques*, vol. 69, no. 11, pp. 4893-4907, Nov. 2021.

[4] N. Zhao *et al.*, "UAV-Assisted Emergency Networks in Disasters," in *IEEE Wireless Communications*, vol. 26, no. 1, pp. 45-51, February 2019.

[5] S. Hayat, E. Yanmaz and R. Muzaffar, "Survey on Unmanned Aerial Vehicle Networks for Civil Applications: A Communications Viewpoint," in *IEEE Communications Surveys & Tutorials*, vol. 18, no. 4, pp. 2624-2661, Fourthquarter 2016.

[6] R. Mudumbai, G. Barriac and U. Madhow, "On the Feasibility of Distributed Beamforming in Wireless Networks," in *IEEE Transactions on Wireless Communications*, vol. 6, no. 5, pp. 1754-1763, May 2007.

[7] K. Alemdar, D. Varshney, S. Mohanti, U. Muncuk, and K. Chowdhury, "RFClock: timing, phase and frequency synchronization for distributed wireless networks," in *Proceedings of the 27th Annual International Conference on Mobile Computing and Networking*, New York, NY, USA, Sep. 2021, pp. 15–27.

[8] Yung-Szu Tu and G. J. Pottie, "Coherent cooperative transmission from multiple adjacent antennas to a distant stationary antenna through AWGN channels," *Vehicular Technology Conference. IEEE 55th Vehicular Technology Conference. VTC Spring 2002*, Birmingham, AL, USA, 2002, pp. 130-134 vol.1.

[9] R. Mudumbai, J. Hespanha, U. Madhow and G. Barriac, "Distributed Transmit Beamforming Using Feedback Control," in *IEEE Transactions on Information Theory*, vol. 56, no. 1, pp. 411-426, Jan. 2010.

[10] H. Ochiai, P. Mitran, H. V. Poor and V. Tarokh, "Collaborative beamforming for distributed wireless ad hoc sensor networks," in *IEEE Transactions on Signal Processing*, vol. 53, no. 11, pp. 4110-4124, Nov. 2005.

[11] C. Wang, Q. Yin, B. Shi, H. Chen and Q. Zou, "Distributed Transmit Beamforming Based on Frequency Scanning," *2011 IEEE International Conference on Communications (ICC)*, Kyoto, Japan, 2011, pp. 1-5.

[12] T. P. Bidigare *et al.*, "Wideband distributed transmit beamforming using channel reciprocity and relative calibration," *2015 49th Asilomar Conference on Signals, Systems and Computers*, Pacific Grove, CA, USA, 2015, pp. 271-275.

[13] J. A. Nanzer, R. L. Schmid, T. M. Comberiate and J. E. Hodkin, "Open-Loop Coherent Distributed Arrays," in *IEEE Transactions on Microwave Theory and Techniques*, vol. 65, no. 5, pp. 1662-1672, May 2017.

[14] M. Badi, N. C. Matson, D. Rajan and J. Camp, "Leveraging UAV Rotation To Increase Phase Coherency in Distributed Transmit Beamforming," *2022 IEEE 19th Annual Consumer Communications & Networking Conference (CCNC)*, Las Vegas, NV, USA, 2022, pp. 445-448.

[15] S. Hanna, E. Krijestorac and D. Cabric, "Destination-Feedback Free Distributed Transmit Beamforming Using Guided Directionality," in *IEEE Transactions on Mobile Computing*, early access, July 5, 2022.

[16] A. Bletsas, A. Lippman and J. N. Sahalos, "Simple, zero-feedback, distributed beamforming with unsynchronized carriers," in *IEEE Journal on Selected Areas in Communications*, vol. 28, no. 7, pp. 1046-1054, September 2010.

[17] C. Pon, "Retrodirective array using the heterodyne technique," in *IEEE Transactions on Antennas and Propagation*, vol. 12, no. 2, pp. 176-180, March 1964.

[18] D. R. Brown III and H. V. Poor, "Time-Slotted Round-Trip Carrier Synchronization for Distributed Beamforming," in *IEEE Transactions on Signal Processing*, vol. 56, no. 11, pp. 5630-5643, Nov. 2008.

[19] R. D. Preuss and D. R. Brown, "Retrodirective distributed transmit beamforming with two-way source synchronization," *2010 44th Annual Conference on Information Sciences and Systems (CISS)*, Princeton, NJ, USA, 2010, pp. 1-6.

[20] R. D. Preuss and D. R. Brown, III, "Two-Way Synchronization for Coordinated Multicell Retrodirective Downlink Beamforming," in *IEEE Transactions on Signal Processing*, vol. 59, no. 11, pp. 5415-5427, Nov. 2011.

[21] G. Fettweis, E. Zimmermann, V. Jungnickel and E. A. Jorswieck, "Challenges in Future Short Range Wireless Systems," in *IEEE Vehicular Technology Magazine*, vol. 1, no. 2, pp. 24-31, 2006.

[22] P. Bidigare *et al.*, "Implementation and demonstration of receiver-coordinated distributed transmit beamforming across an ad-hoc radio network," *2012 Conference Record of the Forty Sixth Asilomar Conference on Signals, Systems and Computers (ASILOMAR)*, Pacific Grove, CA, USA, 2012, pp. 222-226.

[23] C. Hayes, A. R. Margetts, C. Martin, H. Nguyen, W. Song and J. Muldavin, "Informed MIMO implementation of distributed transmit beamforming for range extension," *2016 IEEE Radio and Wireless Symposium (RWS)*, Austin, TX, USA, 2016, pp. 256-258.

[24] S. Leak *et al.*, "Distributed Transmit Beamforming Expanding the Capacity and Range of Tactical Communications," *2018 Military Communications and Information Systems Conference (MilCIS)*, Canberra, ACT, Australia, 2018, pp. 1-6.

[25] M. M. Rahman, H. E. Baidoo-Williams, R. Mudumbai and S. Dasgupta, "Fully wireless implementation of distributed beamforming on a software-defined radio platform," *2012 ACM/IEEE 11th International Conference on Information Processing in Sensor Networks (IPSN)*, Beijing, China, 2012, pp. 305-315.

[26] F. Quitin, U. Madhow, M. M. U. Rahman and R. Mudumbai, "Demonstrating distributed transmit beamforming with software-defined radios," *2012 IEEE International Symposium on a World of Wireless, Mobile and Multimedia Networks (WoWMoM)*, San Francisco, CA, USA, 2012, pp. 1-3.

[27] S. Mohanti *et al.*, "AirBeam: Experimental Demonstration of Distributed Beamforming by a Swarm of UAVs," *2019 IEEE 16th International Conference on Mobile Ad Hoc and Sensor Systems (MASS)*, Monterey, CA, USA, 2019, pp. 162-170.

[28] S. Hanna and D. Cabric, "Distributed Transmit Beamforming: Design and Demonstration From the Lab to UAVs," in *IEEE Transactions on Wireless Communications*, early access, August 18, 2022.

[29] B. Peiffer, R. Mudumbai, S. Goguri, A. Kruger and S. Dasgupta, "Experimental demonstration of retrodirective beamforming from a fully wireless distributed array," *MILCOM 2016 - 2016 IEEE Military Communications Conference*, Baltimore, MD, USA, 2016, pp. 442-447.

[30] P. Chatterjee and J. A. Nanzer, "A study of coherent gain degradation due to node vibrations in open loop coherent distributed arrays," *2017 USNC-URSI Radio Science Meeting (Joint with AP-S Symposium)*, San Diego, CA, USA, 2017, pp. 115-116.

[31] S. M. Ellison, S. R. Mghabghab and J. A. Nanzer, "Multi-Node Open-Loop Distributed Beamforming Based on Scalable, High-Accuracy Ranging," in *IEEE Sensors Journal*, vol. 22, no. 2, pp. 1629-1637, Jan. 15, 2022.
[32] G. Sklivanitis and A. Bletsas, "Testing zero-feedback distributed beamforming with a low-cost SDR testbed," *2011 Conference Record of the Forty Fifth Asilomar Conference on Signals, Systems and Computers (ASILOMAR)*, Pacific Grove, CA, USA, 2011, pp. 104-108.
[33] Y. Shi, R. Enami, J. Wensowitch and J. Camp, "UABeam: UAV-Based Beamforming System Analysis with In-Field Air-to-Ground Channels," *2018 15th Annual IEEE International Conference on Sensing, Communication, and Networking (SECON)*, Hong Kong, China, 2018, pp. 1-9.
[34] S. G. Sanchez, S. Mohanti, D. Jaisinghani and K. R. Chowdhury, "Millimeter-Wave Base Stations in the Sky: An Experimental Study of UAV-to-Ground Communications," in *IEEE Transactions on Mobile Computing*, vol. 21, no. 2, pp. 644-662, 1 Feb. 2022.
[35] S. Suman, S. De, R. K. Mallik, M. Elkashlan and A. Nallanathan, "Beamforming-Based Mitigation of Hovering Inaccuracy in UAV-Aided RFET," in *IEEE Transactions on Communications*, vol. 70, no. 4, pp. 2691-2706, April 2022.
[36] S. Garcia Sanchez and K. R. Chowdhury, "Robust 60-GHz Beamforming for UAVs: Experimental Analysis of Hovering, Blockage, and Beam Selection," in *IEEE Internet of Things Journal*, vol. 8, no. 12, pp. 9838-9854, June 15, 2021.
[37] A. A. Khuwaja, Y. Chen, N. Zhao, M. -S. Alouini and P. Dobbins, "A Survey of Channel Modeling for UAV Communications," in *IEEE Communications Surveys & Tutorials*, vol. 20, no. 4, pp. 2804-2821, Fourthquarter 2018.
[38] J. G. Proakis, *Digital Communications*, 3rd ed. New York, NY, USA: McGraw Hill, 1995.
[39] S. M. Kay, *Fundamentals of Statistical Signal Processing: Estimation Theory*. Upper Saddle River, NJ, USA: Prentice Hall, 1993.
[40] R. Mudumbai, U. Madhow, R. Brown and P. Bidigare, "DSP-centric algorithms for distributed transmit beamforming," *2011 Conference Record of the Forty Fifth Asilomar Conference on Signals, Systems and Computers (ASILOMAR)*, Pacific Grove, CA, USA, 2011, pp. 93-98.
[41] F. Quitin, M. M. U. Rahman, R. Mudumbai and U. Madhow, "A Scalable Architecture for Distributed Transmit Beamforming with Commodity Radios: Design and Proof of Concept," in *IEEE Transactions on Wireless Communications*, vol. 12, no. 3, pp. 1418-1428, March 2013.
[42] Jackson Labs, "LC_XO TCXO Low Cost 1x1 Inch GPSDO Module Spec - gen-2," 1009302-g2 datasheet, Dec. 2018.
[43] Jackson Labs, "LC_XO OCXO Low Cost Ultra Small GPSDO Module Spec - gen-2," 1009301-g2 datasheet, Dec. 2018.
[44] CTS Electronic Components, "Model 525 Temperature Compensated Crystal Oscillator," Document No. 008-0334-0 Revision B, May 2011.

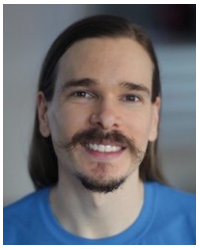

Michael Wentz received the B.S. degree in electrical engineering from Virginia Polytechnic Institute and State University in 2009 and the M.S. degree in electrical and computer engineering from Northeastern University in 2015. He is currently pursuing the Ph.D. degree in electrical engineering at Northeastern University. He is a Lincoln Scholar at MIT Lincoln Laboratory and was previously a Lead Communications Engineer at The MITRE Corporation. His research interests include array signal processing, applications of machine learning for wireless communications, algorithm implementation, and software-defined radio.

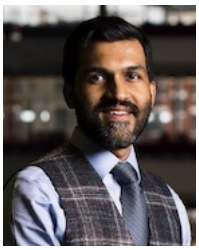

Kaushik Roy Chowdhury (Senior Member, IEEE) received the M.S. degree from the University of Cincinnati in 2006 and the Ph.D. degree from the Georgia Institute of Technology in 2009. He was an Assistant Professor (2009–2015) and an Associate Professor (2015–2020) at Northeastern University, where he is currently a Professor with the Department of Electrical and Computer Engineering. He was the winner of the Presidential Early Career Award for Scientists and Engineers (PECASE) in 2017, the ONR Director of Research Early Career Award in 2016, and the NSF CAREER Award in 2015. His current research interests include dynamic spectrum access, wireless RF energy harvesting and the IoT, and in the area of intra/on-body communication.